RSC Advances

PAPER

View Article Online
View Journal | View Issue

Cite this: *RSC Adv.*, 2017, **7**, 38444

Porous Au/ZnO nanoparticles synthesised through a metal organic framework (MOF) route for enhanced acetone gas-sensing

Jia Xia, Kaidi Diao, Zhou Zheng and Xudong Cui*

The design of porous metal oxides with noble metal doping has attracted tremendous attention due to their vital importance for gas sensing applications. Herein, we report the synthesis of porous Au/ZnO nanoparticles (NPs) through a facile metal organic framework (MOF) route. The structures, sensing properties, as well as sensing mechanisms of products are carefully investigated. The porous Au/ZnO NPs show a high gas-sensing response (17.1 ppm^{-1}) and selectivity towards low concentration acetone at an optimum temperature of 275 °C. The enhanced sensing performances are ascribed to the chemical and electronic sensitization of Au NPs, the porous structure and the high specific surface area of Au/ZnO NPs. Our studies might provide a simple MOF-derived method to synthesize porous structures with noble metal doping and would be beneficial to the development of high performance gas sensing materials.

Received 15th June 2017
Accepted 30th July 2017

DOI: 10.1039/c7ra06690b

rsc.li/rsc-advances

1. Introduction

Volatile organic compound (VOC) gas sensors have received considerable attention due to the increasing needs for health care and environmental protection.[1,2] Metal oxide semiconductors (MOSs) such as ZnO are promising gas sensing materials due to their low cost and high response.[3,4] The sensing performance of MOSs is mainly determined by their chemical composition and microstructure.[5] Over the past decades, various architectures of MOSs have been proposed to exploit their gas-sensing properties.[6,7] With the development of chemical synthesis routes, MOSs with porous nanostructures have attracted widespread interest for their rich exposed active sites, ultra large specific surface areas and the benefit to the diffusion of gases.[8,9] The features of porous structures allow us to achieve high sensing performance. One of the critical issues to obtain such MOSs porous nanostructures is the design of a synthetic route.

Metal–organic frameworks (MOFs) are the ideal self-sacrificial templates to synthesize porous materials through self-template synthetic route, which is attractive due to its low costs and facile synthesis procedures.[10] MOFs are a new family of inorganic–organic hybrid materials with well-defined pores, high specific surface areas and open-metal sites,[11,12] have been widely applied in gas adsorption, catalysis, gas sensing and drug delivery.[13–17] The well-developed pores of MOFs could provide efficient access for small molecules and ions entering and leaving in transformed process, meanwhile the organic linkers could be easily decomposed into gas molecules, leading to the formation of porous nanostructures.[18] Recently, MOFs have been used as self-sacrificial templates to construct porous MOSs with intriguing properties in gas sensor field. For example, the porous $ZnO/ZnCo_2O_4$ hollow core–shell nanocages using ZIF-8 (a kind of zeolitic imidazolate framework)/Co–Zn hydroxide core–shell nanostructure as self-sacrificial precursor showed a gas response of 34.26 to 100 ppm xylene at 320 °C.[19] The Cu-based MOF (HKUST-1) derived porous octahedral Cu_2O/CuO cages exhibited a response of 6.6 to 200 ppm ethanol at 150 °C operating temperature.[20]

Besides the porous nanostructures, the introduction of noble metals in MOSs has been proven to be effective to enhance gas sensing performance.[21,22] Noble metals especially Au NPs are commended for their unique catalytic and electronic activities, and the hybrid nanostructures formed from Au and MOSs have attracted great attention for their enhanced functionalities coming from each component.[23] Considering the effect of Au NPs and porous microstructure, it is reasonable to expect that porous Au/ZnO composites can be a good candidate for low-concentration VOCs sensing materials.

In this work, we present a facile strategy to synthesize porous Au/ZnO composites through a MOF route. The as-prepared Au NPs is attached to the ZIF-8 to construct Au/ZIF-8 NPs, and then the Au/ZIF-8 NPs are used as self-template to synthesize Au/ZnO NPs by direct pyrolysis. Also, a comparative study between the gas sensors based on porous Au/ZnO NPs and ZnO NPs is performed. Our results display that such porous Au/ZnO NPs present enhanced sensing performance in detecting low concentration of gaseous acetone compared with pure ZnO NPs and some presently published results, suggesting the intriguing perspectives of this MOF-driven synthetic route in developing gas-sensing materials with desired properties.

Institute of Chemical Materials, CAEP, Mianyang, Sichuan, China, 621900. E-mail: xudcui@caep.cn

2. Experimental section

2.1 Materials

2-Methylimidazole (2-MeIM) was obtained from Shanghai Macklin Biochemical Co., Ltd., China. Zinc nitrate hexahydrate ($Zn(NO_3)_2 \cdot 6H_2O$), sodium borohydride ($NaBH_4$), tetraoctylammonium bromide (TOAB), 4-dimethylaminopyridine (DMAP) as well as other chemicals were purchased from Aladdin Industrial Corporation. All chemicals were with analytical reagent grades and directly used without further purification.

2.2 Fabrication of Au/ZnO NPs

2.2.1 Fabrication of Au NPs. The preparation method of Au NPs was similar to the related work.[24] 30 mL $HAuCl_4 \cdot 4H_2O$ aqueous solution (30 mmol L^{-1}) was mixed with an 80 mL solution of TOAB in toluene (25 mmol L^{-1}). After stirring for 3 min, a fresh 25 mL $NaBH_4$ aqueous solution (0.4 mol L^{-1}) was added. After further stirring for 2 h, the organic layer was extracted and washed with 0.1 mol L^{-1} sulfuric acid, 0.1 mol L^{-1} sodium hydroxide and deionized water subsequently, and dried over anhydrous sodium sulfate. Then the DMAP aqueous solution (0.1 mol L^{-1}) with equal volume was added, after standing for 2 h, the Au NPs in aqueous phase were obtained.

2.2.2 Fabrication of ZIF-8 and Au/ZIF-8 NPs. 80 mL 2-MeIM aqueous solution (3.1 mol L^{-1}) was mixed with 80 mL $Zn(NO_3)_2 \cdot 6H_2O$ aqueous solution (0.05 mol L^{-1}) under magnetic stirring for 10 min. The products ZIF-8 NPs were collected by centrifugation, purified by washing with deionized water and then dried at 80 °C to get the powder. The Au/ZIF-8 NPs were obtained by directly mixing 0.5 mL solution of the Au NPs and 10 mL aqueous solution containing 0.05 g ZIF-8 powders under stirring for 5 h.

2.2.3 Fabrication of ZnO and Au/ZnO NPs. The as-synthesized ZIF-8 and Au/ZIF-8 NPs powder were calcined at 500 °C in air for 2 h with the heating rate of 1 °C min^{-1}, respectively, and the ZnO and Au/ZnO NPs were obtained.

2.3 Characterization

Transmission electron microscopy (TEM) images were obtained by using a Tecnai G2 F20 S-TWIN microscope with the dispersive X-ray spectroscopy (EDS) under 200 kV accelerating voltage. Field-emission scanning electron microscope (FE-SEM) was performed on a Hitachi S-4800 microscope at 5 kV. Powder X-ray diffraction (PXRD) patterns were recorded on a BRUCKER D8 diffractometer using Cu Kα radiation in the 2θ range from 10° to 90°. Thermal stability was examined by thermogravimetric analysis (TGA, Q500) in flowing air ambient with a ramp rate of 10 °C per minute, heated from 20 to 900 °C. N_2 sorption measurements were conducted on a Micromeritics 2020 analyzer at 77 K.

2.4 Gas sensor characterization

The gas sensors were fabricated as the following steps. The as-synthesized products were mixed with deionized water and ground in an agate mortar to form homogeneous pastes, which were coated on ceramic substrates with Au interdigitated electrodes. Then, the sensors were dried in air overnight and aged at 400 °C for 12 h. The gas-sensing experiments were similar to a previous work and conducted on a CGS-4TP commercial sensor test system (Elite Tech Co. Ltd.) which could export the resistance of samples in real-time.[25] The targeted gases with a certain concentration were obtained by mixing synthetic air and standard gas in a proper ratio controlled by the mass flow controllers (MFC). Firstly, the sensor was exposed to the air which was injected into the test chamber in 1000 cubic centimeters per minute (sccm) by MFC. When the sensor resistance became stable, the target gas was injected into the chamber. Then the other sensor resistance could be obtained. The sensor response is defined as R_{gas}/R_{air} for oxidizing gas and R_{air}/R_{gas} for reducing gas, where R_{air} and R_{gas} are the sensor resistances in the air and in the target gas, respectively. The response and recovery time is defined as the time required for the sensor response reaching 90% of its maximum value and 10% of its minimum value.

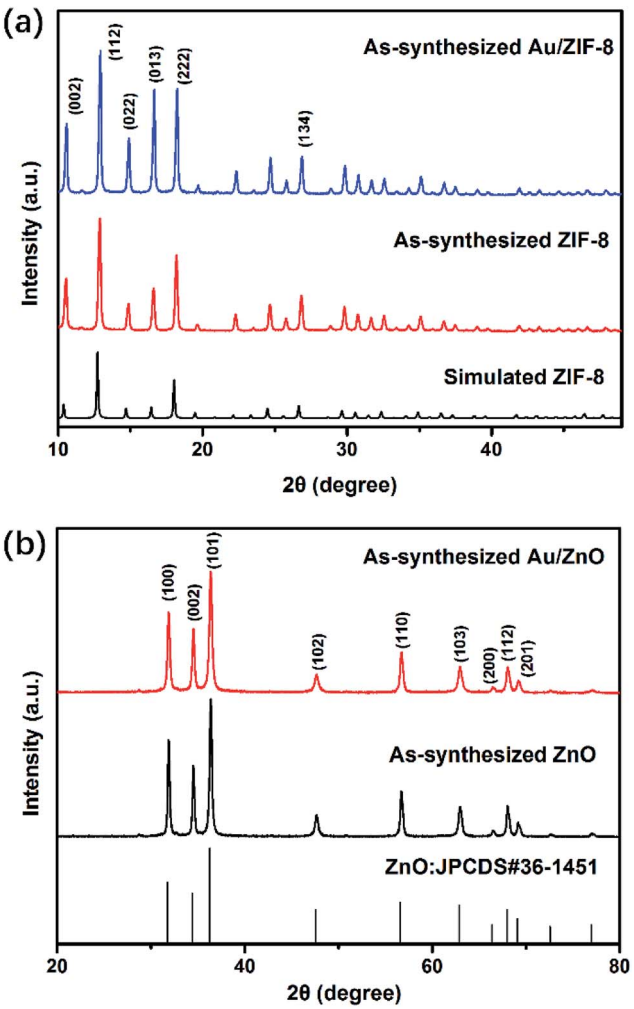

Fig. 1 (a) PXRD patterns of ZIF-8 NPs and Au/ZIF-8 NPs; (b) PXRD patterns of ZnO NPs and Au/ZnO NPs.

3. Results and discussions

3.1 Structural and morphological characterization

We performed PXRD analysis of the as-prepared products to investigate the phase composition and purity. Fig. 1a shows the PXRD patterns of the as-synthesized ZIF-8 and Au/ZIF-8 NPs both match well with the simulated PXRD date of ZIF-8, suggesting that the Au/ZIF-8 has the same crystalline structure as the pristine ZIF-8.[26] Fig. 1b exhibits the PXRD patterns of the ZnO and Au/ZnO, in which all the diffraction peaks fit well with the wurtzite structured ZnO (JCPDS no. 36-1451) with lattice parameters $a = b = 0.324$ nm and $c = 0.520$ nm. No other clear peaks corresponding to impurity phase were detected, indicating that the product had a high purity. The characteristics peaks related to Au peaks were not clearly observed in the PXRD analysis due to the low loading amount of the Au NPs.

As sacrificial templates, ZIF-8 NPs are of great significance in the fabrication of Au/ZnO NPs. The typical morphological features of as-synthesized ZIF-8 and Au/ZIF-8 nanocrystals are shown in Fig. 2. The FESEM image (Fig. 2a) reveals that the prepared pristine ZIF-8 templates exhibit 3-D cubic morphologies with truncated edges, the enlarged TEM image (Fig. 2b)

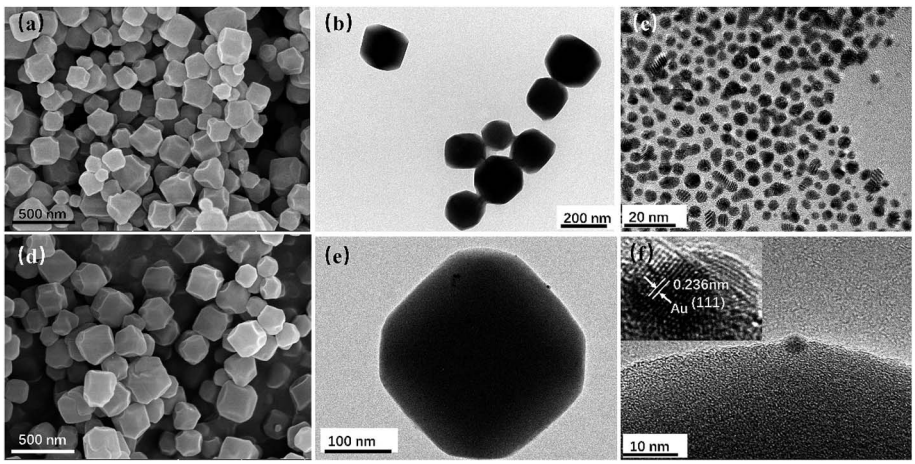

Fig. 2 SEM (a) and TEM (b) images of ZIF-8 NPs; (c) TEM image of Au NPs; SEM (d), TEM (e) and HRTEM (f) images of Au/ZIF-8 NPs.

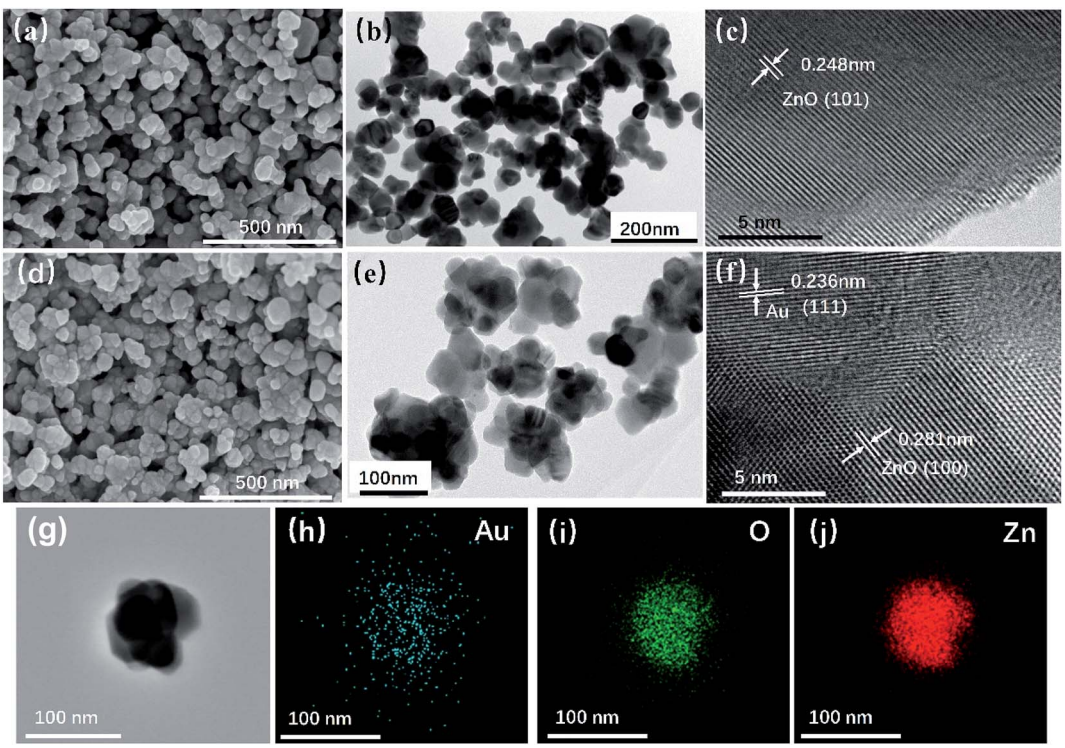

Fig. 3 SEM (a), TEM (b) and HRTEM (c) images of ZnO NPs; SEM (d), TEM (e) and HRTEM (f) images of Au/ZnO NPs; (g–j) EDS elemental mapping images of Au/ZnO NPs.

shows the average diameter of ZIF-8 NPs is about 200 nm. Fig. 2c exhibits the TEM image of the obtained Au NPs with an average size of 5 nm. Therefore, Au NPs could not enter into the ZIF-8 with an inner cavity dimensions of about 1.2 nm.[27] Fig. 2d–f show the SEM and TEM images of Au/ZIF-8 NPs, it can be observed that Au NPs were successfully attached to the surface of ZIF-8 crystal. The corresponding high-resolution transmission electron microscopy (HRTEM) image displays the lattice interlayer distance of 0.236 nm, which is attributed to (111) plane of Au.

Fig. 3 shows the SEM and TEM images of the prepared ZnO and Au/ZnO NPs, which were obtained by the thermal decomposition of ZIF-8 and Au/ZIF-8 NPs. It could be seen that the ZnO NPs (Fig. 3a and b) and Au/ZnO NPs (Fig. 3d and e) are seemingly constructed by ultrafine interpenetrated NPs. The HRTEM images (Fig. 3c–f) reveal lattice interlayer distances of 0.248 nm and 0.281 nm that attributed to the (101) and (100) facets of hexagonal wurtzite phase of ZnO, meanwhile the distance of 0.236 nm is assigned to the (111) crystal plane of Au. Furthermore, the results of EDS elemental mapping (Fig. 3g–j) confirm that the Au NPs are well distributed in ZnO. ZIF-8 NPs are composed of 2-MeIM as bridged organic linkers and $Zn_4(O)$ tetrahedron as secondary building units. In the converted process, the organic linkers of ZIF-8 burned-out and released gases, resulting in the formation of pores. Meanwhile, Zn metal ions reacted with O_2 and converted into ZnO NPs. All the above results suggest that the Au/ZnO NPs were successfully prepared.

Thermogravimetric analysis (TGA) of ZIF-8 and Au/ZIF-8 NPs were conducted to investigate the thermal stability and the decomposition temperature (Fig. 4a). The total mass loss of ZIF-8 is about 64.1%, which is related to the mass loss when ZIF-8 decomposed to ZnO (64.2%). The TGA characteristics of Au/ZIF-8 NPs is similar with ZIF-8 NPs. Such a high weight loss indicates that the organic linkers of ZIF-8 were oxidized into gases and escaped, leading to inter-connected channels of the final ZnO product and being helpful to enhance gas molecules diffusing in gas-sensing process. The major mass loss was recorded under 500 °C. Consequently, the ZIF-8 and Au/ZIF-8 NPs were calcinated to prepare ZnO and Au/ZnO NPs at 500 °C in air. The N_2 desorption–desorption isotherms of ZnO and Au/ZnO NPs were measured to evaluate the specific surface area (Fig. 4b). Both ZnO and Au/ZnO NPs show a representative type IV isotherm under the IUPAC classification with a type H_3 loop, suggesting the existence of mesoporous structure. The abrupt increase at a high relative pressure could be attributed to multilayer adsorption in the macropores.[28] The Brunauer–Emmett–Teller (BET) surface areas of ZnO NPs is ~35 m^2 g^{-1}, close to Au/ZnO NPs (~36 m^2 g^{-1}), implying that the existence of Au NPs has negligible influences on the surface areas and porous structures. Moreover, the high specific areas and porous structures of both ZnO and Au/ZnO NPs due to the porous self-sacrificial ZIF-8 may supply abundant exposed sites, facilitating gas adsorption–desorption and interfacial charge transfer in gas-sensing process.[29]

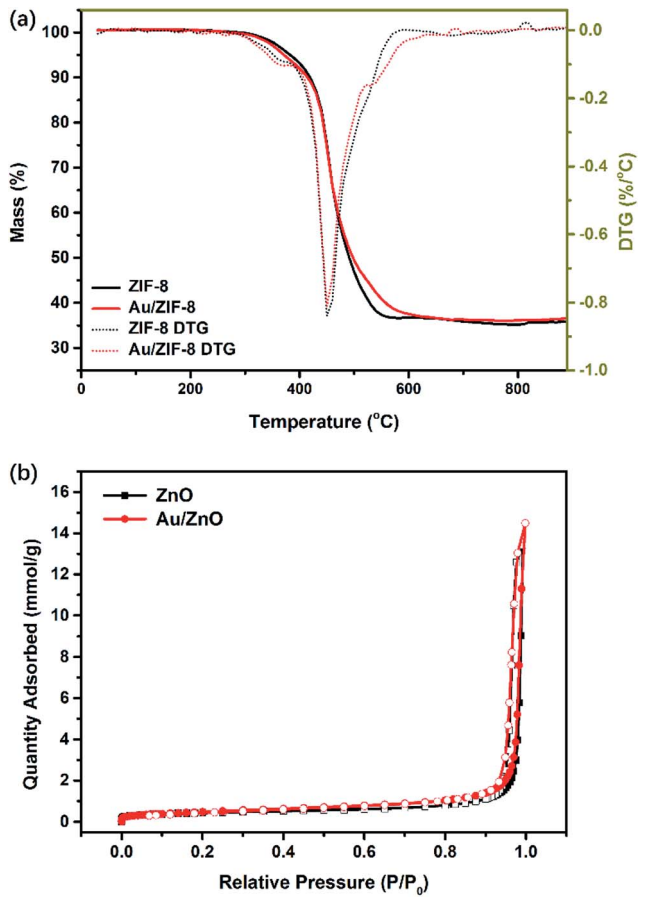

Fig. 4 (a) TGA and DTG analysis of ZIF-8 NPs and Au/ZIF-8 NPs; (b) N_2 adsorption–desorption isotherms of ZnO NPs and Au/ZnO NPs.

3.2 Gas-sensing characteristics

In order to explore the potential application in low-concentration gas-sensing fields, the as-prepared porous ZnO and Au/ZnO NPs were used as sensing materials to fabricate gas sensors, and their gas sensing performances were investigated at the concentration range of sub-ppm to ppm. The sensing properties of MOS sensors are strongly affected by the operating temperature. Fig. 5a shows the electrical resistance response of the porous ZnO and Au/ZnO NPs to 1 ppm acetone at various operating temperatures (200 °C to 400 °C), respectively. It can be clearly seen that optimum operating temperature of both ZnO and Au/ZnO NPs are 275 °C. The responses of sensors based on ZnO and Au/ZnO NPs display the "increase–maximum–decrease" tendency along with the temperature increases, which mainly attributed to the kinetics and mechanics of gas adsorption and desorption on the surface of ZnO.[18,30] At a relatively lower temperature, the diffusion of gas molecules is low and the acetone molecules do not have enough thermodynamic energy to react with the surface adsorbed O^{2-}, O^- or O_2^- species, leading to a low acetone response. When the temperature increases, the higher acetone molecules activity makes the sensing response enhance. With the temperature further increasing, acetone molecules with excessive thermal energy can be easily escaped, leading to the enhancement of gas desorption. Meanwhile, the gas adsorption ability would be restricted because of its exothermic feature, leading to a decreased response.

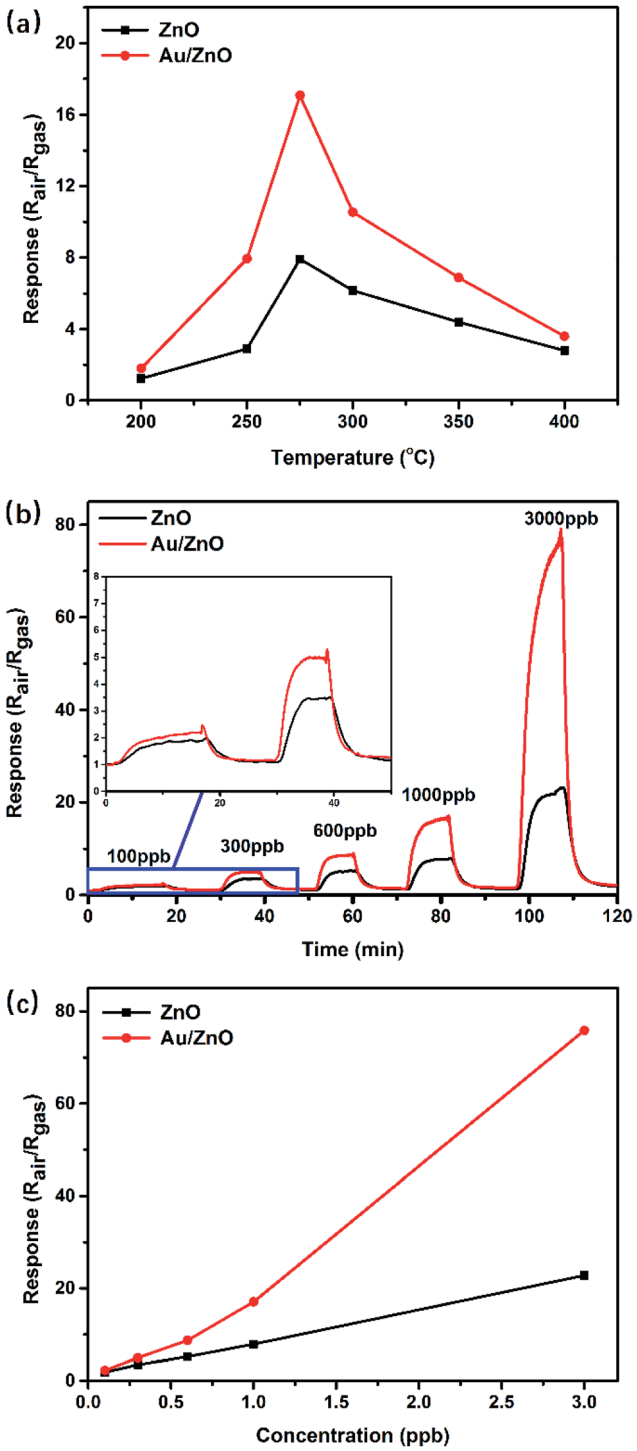

Fig. 5 (a) Responses of ZnO NPs and Au/ZnO NPs towards 1 ppm acetone at different operating temperatures; (b) responses of ZnO NPs and Au/ZnO NPs *versus* acetone concentration in the range of 100–3000 ppb at 275 °C; (c) responses of ZnO NPs and Au/ZnO NPs as a function of acetone concentration.

The dynamic resistance behaviors of the sensors were measured at the optimal operating temperature (275 °C). Fig. 5b depicts the comparative real-time response–recovery curves of the ZnO and Au/ZnO NPs to low-concentration acetone at a range of 100–3000 ppb. It can be found that the corresponding responses increased to equilibrium values when sensors were exposed to acetone and decreased to the baseline when sensors were exposed to air, suggesting a typical feature of n-type semiconductor materials to a reducing gas. Fig. 5c displays the response comparison between ZnO and Au/ZnO as the acetone concentration varying from 100 ppb to 3000 ppb. More gas molecules would react with the adsorbed oxygen species when the concentration increased, leading to enhanced responses. In contrast with the porous ZnO NPs, Au/ZnO NPs perform obviously enhanced responses to acetone at each concentration. Taking the case of 1000 ppb acetone as an example, the corresponding response of ZnO NPs is 7.9 while Au/ZnO NPs is 17.1. The values of response and recovery time were also investigated for their significance in practical applications. Table 1 shows the response and recovery time of porous ZnO and Au/ZnO NPs towards various concentration acetone at 275 °C. For instance, the response and recovery time of porous Au/ZnO NPs is respectively to be 247 s and 209 s for 600 ppb acetone, shorter than 281 s and 318 s of porous ZnO NPs. This may be ascribed to the existence of Au NPs, which enhances the surface adsorption–desorption kinetics of acetone and produces relatively shorter response and recovery time.

Table 1 Response and recovery time of ZnO and Au/ZnO NPs towards different acetone gas concentrations at 275 °C operating temperature

Sample	Concentration (ppb)	Response time (s)	Recovery time (s)
ZnO	100	550	311
	300	310	309
	600	281	318
	1000	270	325
	3000	312	338
Au/ZnO	100	432	255
	300	265	206
	600	247	209
	1000	231	215
	3000	310	220

Selectivity for a target gas is another important parameter to evaluate the performance. The response of porous ZnO and Au/ZnO NPs towards 1 ppm concentration of acetone, ethanol, methanol, carbon monoxide, hydrogen, sulfur dioxide, nitrogen dioxide were measured at their optimal temperature (275 °C) to investigate the selectivity of the as-synthesized gas-sensing materials (Fig. 6a). Evidently, the sensor based on Au/ZnO NPs has a nearly five or more times larger response to acetone than other tested gases, suggesting that this sensor has a great selectivity to acetone. In addition, the other significant gas-sensing parameter of reproducibility was also investigated at 275 °C with 500 ppb acetone. Fig. 6b shows the porous Au/ZnO sensor has good response stability after five on–off cycles. Here, in Table 2, we did a comparison of sensing performances between our Au/ZnO NPs and some previously reported work about acetone sensing. It could be seen that our Au/ZnO NPs perform greater response than other structures, demonstrating

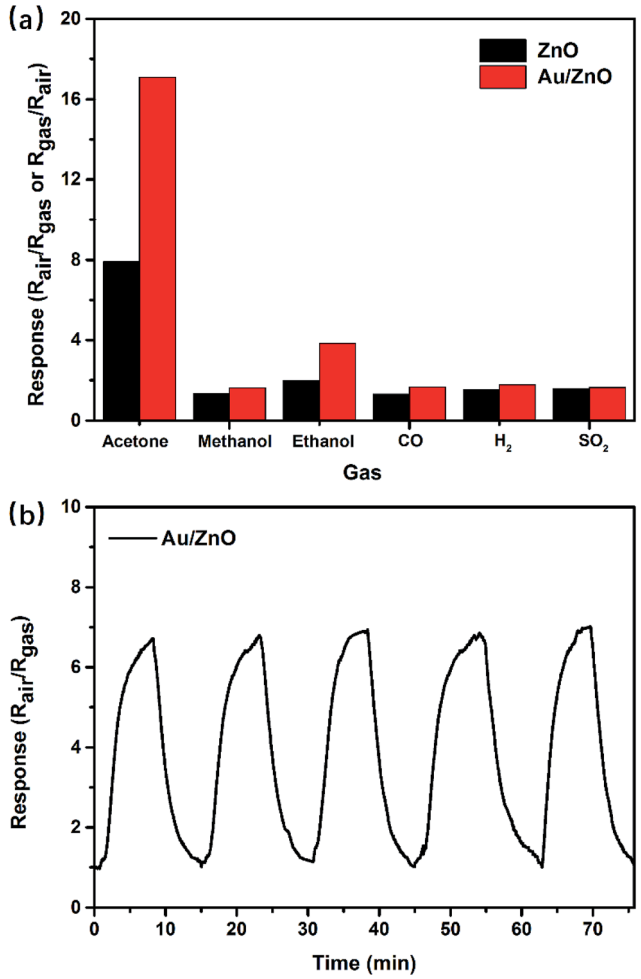

Fig. 6 (a) Responses of ZnO NPs and Au/ZnO NPs towards various tested gases (1 ppm) at 275 °C; (b) response reproducibility of Au/ZnO NPs at 275 °C with 500 ppb gaseous acetone.

that our Au/ZnO NPs may be suitable for acetone sensing with high response and high selectivity.

3.3 Gas-sensing mechanism

A popular and widely accepted sensing mechanism of MOS is based on the change in thickness of surface electron depletion layers when exposed to different types of gases, resulting in resistance change of the sensor.[31] ZnO as a n-type semiconductor, oxygen molecules are chemisorbed onto its surfaces when exposed to the ambient, the free electrons are captured from conduction band to form more active oxygen species including O^{2-}, O^- or O_2^-. As a result, the surface electron depletion layers of ZnO grain boundary are thickened, leading to the reduction of electrons concentration and the increase of resistance.[32] When ZnO is exposed to gases atmosphere such as acetone, chemical reactions between the adsorbed surface oxygen species and the acetone molecules would release electrons which trapped in the ionized oxygen species back into the conduction band. Hence, the width of surface depletion region is reduced, resulting in the decrease of resistance.[33] The related reactions can be summarized as follows.[34]

$$O_{2(gas)} \rightarrow O_{2(ads)} \quad (1)$$

$$O_{2(ads)} + e^- \rightarrow O_2^-{}_{(ads)} \quad (2)$$

$$O_2^-{}_{(ads)} + e^- \rightarrow 2O^-{}_{(ads)} \quad (3)$$

$$CH_3COCH_3 + 8O^-{}_{(ads)} \rightarrow 3CO_2 + 3H_2O + 8e^- \quad (4)$$

The enhanced gas-sensing properties of Au/ZnO composites could be ascribed to the chemical and electronic sensitization provided by Au NPs (Fig. 7a). In the case of chemical sensitization, the well-known catalytic and spillover effects of Au NPs are advantageous for gas sensing process. The sensing performance of gas sensors is usually influenced by the ability of absorbing and ionizing oxygen species. Au NPs could offer preferred adsorption and activation sites to bind and dissociate oxygen molecules, leading to the increase of absorbed oxygen species quantity. In consequence, more electrons would be extracted from conduction band and the baseline resistance of ZnO would increase in air atmosphere, which is conductive to enhance the response (R_{air}/R_{gas}).[35] In addition, Au NPs could break acetone into activated fragments which are spilled over onto the semiconductor to react with the surface absorbed oxygen species readily. Therefore the reaction between acetone and ZnO is accelerated and the response time is reduced.[36]

In the case of electronic sensitization, the Au NPs in ZnO will form the Schottky junction between Au and ZnO, which involves

Table 2 Comparison of ZnO-based sensor performances towards acetone in various work

Materials	Acetone (ppm)	Temperature (°C)	Response (ppm)	Reference
Hierarchical hollow ZnO nanocage	1	300	14.8	29
Core–shell Au@ZnO nanoparticles	5	300	21.65	37
La_2O_3-doped flowerlike ZnO structures	10	350	7.6	34
Ag doped ZnO nanoneedles	200	370	30.3	38
ZnO@ZIF–CoZn nanofibers	100	260	84	39
ZnO/$ZnFe_2O_4$ hollow nanocages	100	290	25.8	40
Au@ZnO yolk shell nanospheres	100	300	37	35
Porous $ZnFe_2O_4$ nanospheres	100	200	42.1	41
Hierarchical porous WO_3 nanofibers having 1D nanoneedles	5	350	18.5	42
Hierarchical porous SnO_2 nanoflowers	20	280	33	43
Au/ZIF-8 derived porous Au/ZnO nanoparticles	1	275	17.1	This work

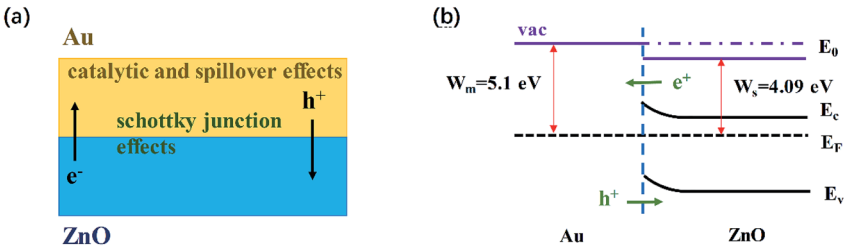

Fig. 7 (a) Schematic representation of the main phenomena beneficially affecting the gas sensing behavior of the Au/ZnO NPs; (b) schematic illustration of the energy band diagram of Au/ZnO.

the modulation and control of Fermi energy levels (Fig. 7b). The work function of Au (5.1 eV) is larger than that of ZnO (4.09 eV), thus the free electrons will be naturally flowed from the conduction band of ZnO to Au, leading to the energy bending.[31] As a result, an electron depletion layer is created at the surface of ZnO and the electron concentration of ZnO is decreased. When the acetone molecules are adsorbed on such Au/ZnO NPs and react with adsorbed oxygen species, more electrons are likely to be released back into the conduction band of ZnO and the response is enhanced.[37] Moreover, the great sensing performance of Au/ZnO NPs is attributed to the porous structure and high specific area. In our work, the distinctive configuration of porous structure and high surface specific area could facilitate the diffusion of oxygen and acetone molecules, and provide more exposed active sites for adsorption of oxygen molecules. Accordingly, the kinetics of the reaction between acetone molecules and adsorbed oxygen species is improved. As described above, due to the electronic and chemical sensitization of Au NPs existed in the Au/ZnO NPs and the unique porous structure and high specific surface area, the sensor based on Au/ZnO NPs displays excellent sensing performance towards low concentration gaseous acetone.

4. Conclusion

The porous Au/ZnO NPs were successfully constructed through a facile strategy, which includes the fabrication of Au/ZIF-8 precursor and subsequent transformation to Au/ZnO NPs by directly calcining in air. The Au/ZnO NPs exhibit enhanced gas sensing performances to acetone when compared to ZnO. The improved sensing performances are related to the chemical and electronic sensitization of Au NPs. Moreover, the high specific area and porous structure of Au/ZnO NPs due to the MOF template could facilitate the redox reaction and thus are conductive to the sensing performance. Our findings supply a simple MOF-derived method to synthesize porous structures with noble metal doping and this would be beneficial to the development of high performance gas sensing materials.

Conflict of interest

The authors declare that they have no conflict of interest to this work.

References

1 I. D. Kim, A. Rothschild and H. L. Tuller, *Acta Mater.*, 2013, **61**, 974.
2 X. Liu, S. Cheng, H. Liu, S. Hu, D. Zhang and H. Ning, *Sensors*, 2012, **12**, 9635.
3 G. F. Fine, L. M. Cavanagh, A. Afonja and R. Binions, *Sensors*, 2010, **10**, 5469.
4 Y. B. Hahn, R. Ahmad and N. Tripathy, *Chem. Commun.*, 2012, **48**, 10369.
5 Y. Feng, L. ShaoBo, M. FanLi, L. JinYun and J. Zhen, *Sensors*, 2012, **12**, 2610.
6 K. Diao, M. Zhou, J. Zhang, Y. Tang, S. Wang and X. Cui, *Sens. Actuators, B*, 2015, **219**, 30.
7 J. Wu, D. Zeng, S. Tian, K. Xu, D. Li and C. Xie, *J. Mater. Sci.*, 2015, **50**, 7725.
8 T. Wagner, S. Haffer, C. Weinberger, D. Klausa and M. Tiemann, *Chem. Soc. Rev.*, 2012, **42**, 4036.
9 J. Huang, C. Shi, G. Fu, P. Sun, X. Wang and C. Gu, *Mater. Chem. Phys.*, 2014, **144**, 575.
10 Y. Lv, L. Gan, M. Liu, W. Xiong, Z. Xu, D. Zhu and D. S. Wright, *J. Power Sources*, 2012, **209**, 152.
11 L. Song, J. Zhang, L. Sun, F. Xu, F. Li, H. Zhang, X. Si, C. Jiao, Z. Li and S. Liu, *Energy Environ. Sci.*, 2012, **5**, 7508.
12 W. Lu, Z. Wei, Z. Y. Gu, T. F. Liu, J. Park, J. Park, J. Tian, M. Zhang and Q. Zhang, *Chem. Soc. Rev.*, 2014, **43**, 5561.
13 d. V. B. Van, B. Bueken, J. Denayer and V. D. De, *Chem. Soc. Rev.*, 2014, **43**, 5766.
14 M. P. Suh, H. J. Park, T. K. Prasad and D. W. Lim, *Chem. Rev.*, 2011, **112**, 782.
15 H. Furukawa, K. E. Cordova, M. O'Keeffe and O. M. Yaghi, *Science*, 2013, **341**, 1230444.
16 V. Stavila, A. A. Talin and M. D. Allendorf, *Chem. Soc. Rev.*, 2014, **43**, 5994.
17 P. Ramaswamy, N. E. Wong and G. K. Shimizu, *Chem. Soc. Rev.*, 2014, **43**, 5913.
18 Y. Lü, W. Zhan, Y. He, Y. Wang, X. Kong, Q. Kuang, Z. Xie and L. Zheng, *ACS Appl. Mater. Interfaces*, 2014, **6**, 4186.
19 F. Qu, H. Jiang and M. Yang, *Nanoscale*, 2016, **8**, 16439.
20 Y. Wang, Y. Lü, W. Zhan, Z. Xie, Q. Kuang and L. Zheng, *J. Mater. Chem. A*, 2015, **3**, 12796.
21 N. S. Ramgir, M. Kaur, P. K. Sharma, N. Datta, S. Kailasaganapathi, S. Bhattacharya, A. K. Debnath,

D. K. Aswal and S. K. Gupta, *Sens. Actuators, B*, 2013, **187**, 313.
22 X. Han, Y. Sun, Z. Feng, G. Zhang, Z. Chen and J. Zhan, *RSC Adv.*, 2016, **6**, 37750.
23 L. Wang, Z. Lou, T. Fei and T. Zhang, *Sens. Actuators, B*, 2012, **161**, 178.
24 K. N. Kim, K. J. Yun, J. Chun, B. U. Ye, M. Gu, E. Seo, S. Kim, S. W. Kim, B. S. Kim and J. M. Baik, *Nano Energy*, 2016, **26**, 360.
25 K. Diao, Y. Huang, M. Zhou, J. Zhang, Y. Tang, S. Wang, T. Liu and X. Cui, *RSC Adv.*, 2016, **6**, 28419.
26 H. Jiang, Q. Yan, R. Chen and W. Xing, *Microporous Mesoporous Mater.*, 2016, **225**, 33.
27 K. S. Park, Z. Ni, A. P. Côté, J. Y. Choi, R. Huang, F. J. Uribe-Romo, H. K. Chae, M. O'Keeffe and O. M. Yaghi, *Proc. Natl. Acad. Sci.*, 2006, **103**, 10186.
28 K. S. W. Sing, *Pure Appl. Chem.*, 1998, **54**, 2201.
29 W. Li, X. Wu, N. Han, J. Chen, X. Qian, Y. Deng, W. Tang and Y. Chen, *Sens. Actuators, B*, 2015, **225**, 158.
30 X. L. Xu, Y. Chen, S. Y. Ma, W. Q. Li and Y. Z. Mao, *Sens. Actuators, B*, 2015, **213**, 222.
31 Q. A. Drmosh and Z. H. Yamani, *Appl. Surf. Sci.*, 2016, **375**, 57.
32 W. T. Koo, S. J. Choi, S. J. Kim, J. S. Jang, H. L. Tuller and I. D. Kim, *J. Am. Chem. Soc.*, 2016, **138**, 13431.
33 I. Lee, S. J. Choi, K. M. Park, S. L. Sun, S. Choi, I. D. Kim and C. O. Park, *Sens. Actuators, B*, 2014, **197**, 300.
34 J. Q. He, J. Yin, D. Liu, L. X. Zhang, F. S. Cai and L. J. Bie, *Sens. Actuators, B*, 2013, **182**, 170.
35 X. Li, X. Zhou, H. Guo, C. Wang, J. Liu, P. Sun, F. Liu and G. Lu, *ACS Appl. Mater. Interfaces*, 2014, **6**, 18661.
36 M. E. Franke, T. J. Koplin and U. Simon, *Small*, 2006, **2**, 36.
37 W. Li, X. Wu, N. Han, J. Chen, W. Tang and Y. Chen, *Powder Technol.*, 2016, **304**, 241.
38 Y. Al-Hadeethi, A. Umar, A. A. Ibrahim, S. H. Al-Heniti, R. Kumar, S. Baskoutas and B. M. Raffah, *Ceram. Int.*, 2017, **43**, 6765.
39 M. S. Yao, W. X. Tang, G. E. Wang, B. Nath and G. Xu, *Adv. Mater.*, 2016, **28**, 5229.
40 X. Wang, S. Zhang, M. Shao, J. Huang, X. Deng, P. Hou and X. Xu, *Sens. Actuators, B*, 2017, **251**, 27.
41 X. Zhou, J. Liu, C. Wang, P. Sun, X. Hu, X. Li, K. Shimanoe, N. Yamazoe and G. Lu, *Sens. Actuators, B*, 2015, **206**, 577.
42 S. J. Choi, C. Choi, S. J. Kim, H. J. Cho, S. Jeon and I. D. Kim, *RSC Adv.*, 2015, **5**, 7584.
43 L. Cheng, S. Y. Ma, T. T. Wang and J. Luo, *Mater. Lett.*, 2015, **143**, 84.